ELSEVIER

Materials Science and Engineering A231 (1997) 1–9

MATERIALS SCIENCE & ENGINEERING A

# Influence of applied electric field and mechanical boundary condition on the stress distribution at the crack tip in piezoelectric materials

Susmit Kumar, Raj N. Singh *

*Department of Materials Science and Engineering, University of Cincinnati, P.O. Box 210012, Cincinnati, OH 45221-0012, USA*

Received 22 May 1996; revised 2 December 1996

**Abstract**

A finite element technique is used to study the stress distributions at the crack tip of a piezoelectric ceramic subject to the applied electric fields. Under a negative applied electric field (electric field opposite to the direction of poling), the assumption of crack surfaces to be free of surface traction as the mechanical boundary condition is found to be invalid. It is shown that the stress distributions at the crack tip under the negative applied electric field are different for the closed crack mechanical boundary condition than those for the traction-free crack surface mechanical boundary condition. © 1997 Elsevier Science S.A.

*Keywords:* Finite element; Fracture mechanics; Piezoelectric; Plane strain; Stress distribution

## 1. Introduction

In piezoelectric materials, the application of an electrical field generates mechanical stresses apart from generating electrical charges and the application of a mechanical load generates electrical charges apart from mechanical stresses. This makes piezoelectric materials very useful in electromechanical and electronic devices such as electromechanical actuators, sensors, and transducers. In these devices, both electrical and mechanical loads are applied on the piezoelectric components which give rise to sufficiently high stresses which can lead to their failure.

In the theoretical analyses of crack problems in the piezoelectric materials, although researchers have different opinions about the electrical boundary conditions at the crack surfaces, they usually consider crack surfaces to be free of surface traction as defined by Eq. (1) to be the mechanical boundary condition:

$$\sigma_{\theta\theta} = \sigma_{r\theta} = \sigma_{\theta z} = 0 \tag{1}$$

where, $r$, $\theta$ and $z$ denote the co-ordinates in the cylindrical co-ordinate system.

* Corresponding author. Tel.: +1 513 5565172; fax: +1 513 5562569; e-mail: rsingh@uceng.uc.edu.


*PII* S0921-5093(97)00038-5

Usually, as the dielectric constant of the air or the medium between the crack faces is very small as compared with that of the piezoelectric material, some researchers [1–8] have assumed: (i) zero dielectric permittivity of the medium between the two crack surfaces; and (ii) the crack surfaces to be free of surface charge as defined by Eq. (2),

$$D_\theta^+ = D_\theta^- = 0 \tag{2}$$

where, $D_\theta$ is the normal electrical displacement at the crack faces. Superscripts + and − denote the upper and lower crack surfaces, respectively.

On the other hand, researchers such as Parton [9], Zhang and Hack [10], Hao and Shen [11], and Dunn [12] have assumed that although the magnitude of the normal electrical displacement component at the crack face is very small, the electrical displacement is continuous across the crack faces. Parton [9] used the electrical boundary conditions as

$$D_\theta^+ = D_\theta^- \tag{3}$$

and

$$\phi^+ = \phi^- \tag{4}$$

where $\phi$ is the electrical potential. Hao and Shen [11] used the boundary condition in which the electric per-

meability of air in a crack gap is considered. Apart from Eq. (3), they used an additional equation for the boundary condition at the crack faces,

$$D_\theta^+ (u_\theta^+ - u_\theta^-) = \varepsilon_a(\phi^- - \phi^+) \tag{5}$$

where $u_\theta$ is the displacement component normal to the crack face and $\varepsilon_a$ is the permittivity of air. If there is no gap between the crack faces, i.e., $u_\theta^+ - u_\theta^- = 0$, then Eq. (5) reduces to Eq. (4) and for the condition $\varepsilon_a = 0$, i.e., for a medium having zero electrical permittivity, Eq. (5) reduces to Eq. (2).

In a recent study, we used the finite element technique to calculate the angular distributions of radial and tangential stresses at the crack tip in piezoelectric materials for the combined mechanical and electrical loads [13], and also the energy release rates for the crack propagation under these conditions [14,15]. The calculated stress distributions and the energy release rates were in agreement with the theoretical results of Sosa [6] and Pak [7], and the experimental results of Wang and Singh [16,17].

In this study, a finite element technique is used to study the validity of the mechanical boundary condition at crack surfaces to be free of traction (Eq. (1)) in piezoelectric materials under applied electric field. The results reported in this paper are calculated using the electrical boundary condition as defined by Eq. (2).

## 2. Constitutive equations

The constitutive equations for the piezoelectric materials are,

$$\sigma_{ij} = C_{ijkl}s_{kl} - e_{kij}E_k \tag{6}$$

$$D_i = e_{ikl}s_{kl} + \varepsilon_{ik}E_k \tag{7}$$

where $\sigma_{ij}$, $s_{kl}$, $E_k$ and $D_i$ are the stress, strain, electric field strength and electric displacement tensors, respectively. $C_{ijkl}$, $E_{ik}$ and $e_{ikl}$ are the elastic constant tensor, the dielectric constants and the piezoelectric constants, respectively, of the material. The strain tensor is related to the displacement vector $\{u_i,\ i = 1,\ 2,\ 3\}$ by the equation,

$$s_{ij} = \frac{1}{2}(u_{i,j} + u_{j,i}) \tag{8}$$

where

$$u_{i,j} = \frac{\partial u_i}{\partial x_j}, \quad x_j = \text{co-ordinate axes}$$

The electric field strength is related to the electrical potential $\phi$ by the equation

$$E_i = -\frac{\partial \phi}{\partial x_i} \tag{9}$$

The governing field equations are given by

$$\sigma_{ij,j} + f_i = 0 \tag{10}$$

$$D_{i,i} = q_b \tag{11}$$

where, $f_i$ and $q_b$ are the body force and body charge, respectively.

The boundary conditions are given by

$$\sigma_{ij}n_j = T_i \tag{12}$$

$$D_i n_i = -q_s \tag{13}$$

where $n_i$ is the unit normal vector to the boundary surface. $T_i$ and $q_s$ are the surface traction and surface charge, respectively, applied on the boundary surface.

Poled piezoelectric materials like barium titanate and lead zirconate titanate (PZT) are transversely isotropic elastic materials with hexagonal symmetry of class 6 mm. The constitutive relations for these materials can be written as (with $x_3$ as the poling direction and $x_1$–$x_2$ plane as the isotropic plane),

$$\begin{Bmatrix} \sigma_{11} \\ \sigma_{22} \\ \sigma_{33} \\ \sigma_{32} \\ \sigma_{31} \\ \sigma_{12} \end{Bmatrix} = \begin{bmatrix} C_{11} & C_{12} & C_{13} & 0 & 0 & 0 \\ C_{12} & C_{11} & C_{13} & 0 & 0 & 0 \\ C_{13} & C_{13} & C_{33} & 0 & 0 & 0 \\ 0 & 0 & 0 & C_{44} & 0 & 0 \\ 0 & 0 & 0 & 0 & C_{44} & 0 \\ 0 & 0 & 0 & 0 & 0 & 1/2(C_{11} - C_{12}) \end{bmatrix} \begin{Bmatrix} s_{11} \\ s_{22} \\ s_{33} \\ 2s_{32} \\ 2s_{31} \\ 2s_{12} \end{Bmatrix} - \begin{bmatrix} 0 & 0 & e_{31} \\ 0 & 0 & e_{31} \\ 0 & 0 & e_{33} \\ 0 & e_{15} & 0 \\ e_{15} & 0 & 0 \\ 0 & 0 & 0 \end{bmatrix} \begin{Bmatrix} E_1 \\ E_2 \\ E_3 \end{Bmatrix} \tag{14}$$

$$\begin{Bmatrix} D_1 \\ D_2 \\ D_3 \end{Bmatrix} = \begin{bmatrix} 0 & 0 & 0 & 0 & e_{15} & 0 \\ 0 & 0 & 0 & e_{15} & 0 & 0 \\ e_{31} & e_{31} & e_{33} & 0 & 0 & 0 \end{bmatrix} \begin{Bmatrix} s_{11} \\ s_{22} \\ s_{33} \\ 2s_{32} \\ 2s_{31} \\ 2s_{12} \end{Bmatrix} + \begin{bmatrix} \varepsilon_{11} & 0 & 0 \\ 0 & \varepsilon_{11} & 0 \\ 0 & 0 & \varepsilon_{33} \end{bmatrix} \begin{Bmatrix} E_1 \\ E_2 \\ E_3 \end{Bmatrix} \tag{15}$$

where $C_{ij}$ and $e_{ij}$ are the elastic constant tensor and the piezoelectric constants, respectively, in the contracted notation. The relationships between the contracted and expanded notations of these variables are given as

$$C_{11} = C_{1111} = C_{2222} \qquad C_{12} = C_{1122}$$
$$C_{13} = C_{1133} = C_{2233} \qquad C_{33} = C_{3333}$$
$$C_{44} = C_{2323} = C_{3131} \qquad C_{66} = C_{1212} = 1/2(C_{11} - C_{12})$$
$$e_{31} = e_{311} = e_{322} \qquad e_{33} = e_{333} \qquad e_{15} = e_{113} = e_{323}$$

For the plane strain conditions ($s_{22} = s_{12} = s_{23} = 0$ and $E_2 = 0$), Eqs. (14) and (15) can be written as,

$$\begin{Bmatrix} \sigma_{11} \\ \sigma_{22} \\ \sigma_{33} \\ \sigma_{31} \end{Bmatrix} = \begin{bmatrix} C_{11} & C_{13} & 0 \\ C_{12} & C_{13} & 0 \\ C_{13} & C_{33} & 0 \\ 0 & 0 & C_{44} \end{bmatrix} \begin{Bmatrix} s_{11} \\ s_{33} \\ 2s_{31} \end{Bmatrix} - \begin{bmatrix} 0 & e_{31} \\ 0 & e_{31} \\ 0 & e_{33} \\ e_{15} & 0 \end{bmatrix} \begin{Bmatrix} E_1 \\ E_3 \end{Bmatrix} \tag{16}$$

$$\begin{Bmatrix} D_1 \\ D_3 \end{Bmatrix} = \begin{bmatrix} 0 & 0 & e_{15} \\ e_{31} & e_{33} & 0 \end{bmatrix} \begin{Bmatrix} s_{11} \\ s_{33} \\ 2s_{31} \end{Bmatrix} + \begin{bmatrix} \varepsilon_{11} & 0 \\ 0 & \varepsilon_{33} \end{bmatrix} \begin{Bmatrix} E_1 \\ E_3 \end{Bmatrix} \tag{17}$$

## 3. Model

In order to study the stress distributions at the crack tip in a piezoelectric material, a double edge-notched (DEN) specimen is modeled. The dimensions of the specimen are shown in Fig. 1. Due to symmetry, only the right half of the model (shown by ABCD) is used in the finite element analysis. Direction shown by P is the poling direction. The crack surface OE is assumed to be perpendicular to the poling direction. A specialized preprocessor is written to divide the model into finite 'elements' taking into consideration the two free surfaces of the crack along OE. In order to accurately calculate the stress distributions at the crack tip, the mesh density is increased near the crack tip. The finite element mesh for the model is shown in Fig. 2(a). Eight-noded quadrilateral finite elements with three degrees of freedom—$u_x$ ($x$-displacement), $u_y$ ($y$-displacement) and $\phi$ (electric potential)—are used in the model. The total number of nodes and elements in the finite element analysis are 4551 and 1488, respectively.

Fig. 2(b) shows the enlarged view of the finite element mesh near the crack tip. The quadrilateral elements at the crack tip are at an interval of 7.5° . Sosa and Pak [4] and Wang [8] theoretically showed that stress and electric fields at the crack tip show classical $1/\sqrt{r}$ type of singularity. In order to produce a $1/\sqrt{r}$ type of singularity for the displacement and electric potential at the crack tip, the three nodes along one of the sides of each of the quadrilateral elements are collapsed at the crack tip and the two adjoining mid-points are moved to the quarter point distances [18]. The angular distributions of the radial and tangential components of stresses at an interval of 7.5° are calculated for the four node sets defined by points along the circular arcs OP, OQ, OR and OS (Fig. 2(c)). The ratios OP/OE, OQ/OE, OR/OE and OS/OE (radial

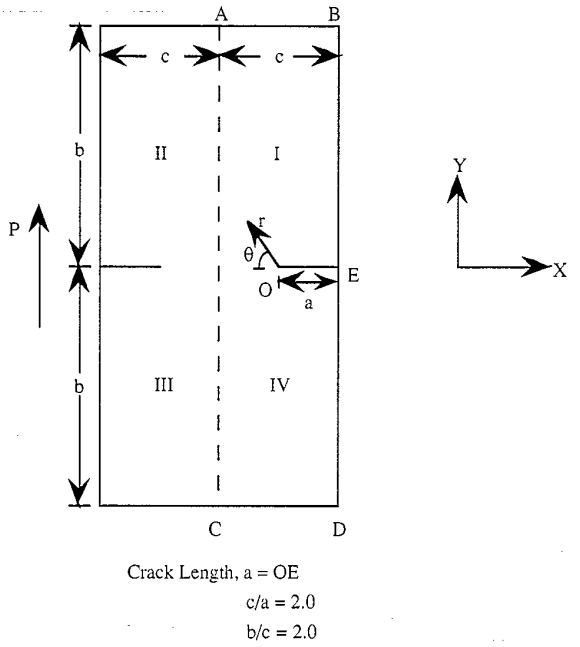


Fig. 1. The double edge-notch (DEN) model in two dimensions. Direction shown by P is the poling direction. Due to symmetry, only half of the double edge-notch specimen, ABCD, has been modeled. For the mechanical boundary conditions, point C was fixed; line CD and line AC were constrained to have displacement only along the $x$-axis and $y$-axis, respectively. For the electrical boundary condition, the line CD was grounded. For the electrical boundary conditions at the crack surfaces, the normal electrical displacement was assumed to be zero.

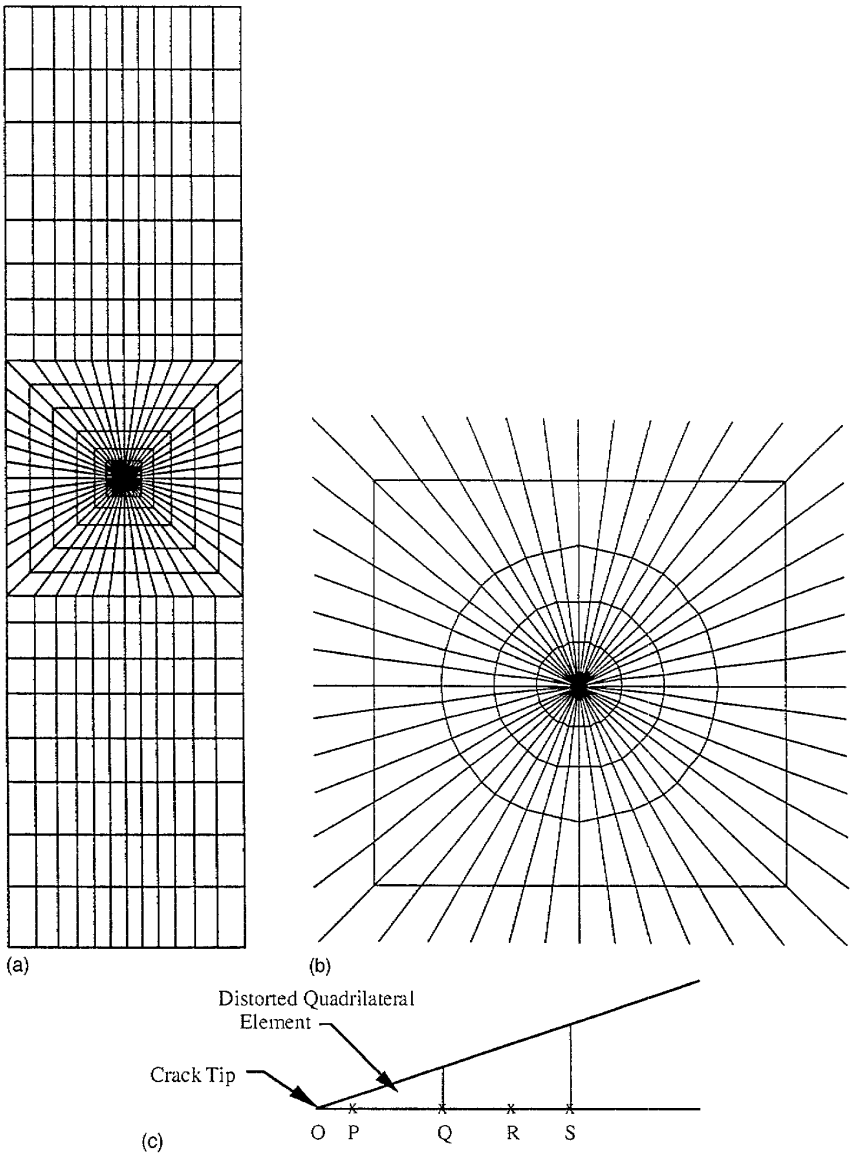


Fig. 2. (a)The finite element mesh for the model. Eight-noded quadrilateral finite elements with three degrees of freedom $u_x$ ($x$-displacement), $u_y$ ($y$-displacement) and $\phi$ (electric potential) were used in the model. The total number of nodes and elements were 4551 and 1488, respectively. (b) The enlarged view of the finite element mesh near the crack tip. The quadrilateral elements at the crack tip were at an interval of 7.5°. (c) The angular distributions of the radial and tangential stresses were calculated for the four node sets defined by the points along the circular arcs OP, OQ, OR and OS. The ratios OP/OE, OQ/OE, OR/OE and OS/OE are $1.0 \times 10^{-5}$, $4.0 \times 10^{-5}$, $6.0 \times 10^{-5}$ and $8.0 \times 10^{-5}$, respectively. OE is the crack length (Fig. 1).

distances in terms of the crack length OE) are $1.0 \times 10^{-5}$, $4.0 \times 10^{-5}$, $6.0 \times 10^{-5}$ and $8.0 \times 10^{-5}$, respectively. The side lengths (in radial direction from the crack tip) of the elements are about 1.25 times the preceding element length (starting from the element at the crack tip) in order to increase the accuracy of the results. Initially, we tried a finite element mesh for which the ratios OP/OE, OQ/OE, OR/OE and OS/OE were $1.25 \times 10^{-4}$, $5.0 \times 10^{-4}$, $7.5 \times 10^{-4}$ and $1.0 \times 10^{-3}$, respectively, but for this mesh, the angular variations of stress distributions calculated for the applied electric field were found to be inaccurate and different from those predicted theoretically by Sosa [6] and Pak [7].

For the mechanical boundary conditions, point C was fixed; lines CD and AC were constrained to have displacement only along the $x$-axis and $y$-axis, respectively. For the electrical boundary condition, the line

CD was grounded, and the normal electrical displacement at the crack surfaces was assumed to be zero. Electric potential was applied on the line AB for creating an electrical load. The finite element package ABAQUS Version 5.4 [19] was used to calculate the stresses at the nodes of the model. Plane strain conditions were assumed for the analysis.

## 4. Results and discussion

The PZT-5H material properties, as given in Table 1, were used for the analysis. The angular distributions of the radial and tangential stresses under applied electric field were calculated for the four node sets defined by points along the circular arcs OP, OQ, OR and OS at an interval of 7.5° (Fig. 2(c)). The stresses were normalized by multiplying them by the factor $\sqrt{2r/a}$, where $r$ and $a$ are the radial distance of the point from the crack tip and crack length, respectively. For applied electric fields, the angular distributions of the stresses differ for the different circular arcs, and only the angular distributions of the stresses for the circular arc defined by the radius OP were found to be accurate and same as those predicted by the theoretical analyses of Sosa [6] and Pak [7]. Hence, a very fine mesh near a crack tip is required to accurately calculate stresses near the crack tip in a piezoelectric material. The angular distributions of stresses reported in this paper are for the circular arc defined by the radius OP which is nearest to the crack tip and at a distance of $1.0 \times 10^{-5}$ of the crack length.

The double edge-notched specimen, as shown in Fig. 1, was used to study the stress distributions at the crack tip under electrical loads. The stress distributions at the crack tip under either a negative or a positive electric potential applied at the top edge AB (Fig. 1) were determined. As the bottom edge CD was grounded, negative electric potential on AB produced an electric field which was parallel to the poling direction. We call this type of electric field a positive electric field. A negative electric field, which was opposite to the poling direction, was produced by the application of a positive electric potential on the edge AB.

Table 1
Material properties for PZT-5H piezoelectric ceramic [7]

| Parameter | |
|---|---|
| $C_{11}$ | $12.6 \times 10^{10}$ N m$^{-2}$ |
| $C_{12}$ | $5.5 \times 10^{10}$ N m$^{-2}$ |
| $C_{13}$ | $12.3 \times 10^{10}$ N m$^{-2}$ |
| $C_{33}$ | $11.7 \times 10^{10}$ N m$^{-2}$ |
| $C_{44}$ | $3.53 \times 10^{10}$ N m$^{-2}$ |
| $e_{31}$ | $-6.5$ C m$^{-2}$ |
| $e_{33}$ | 23.3 C m$^{-2}$ |
| $e_{15}$ | 17.0 C m$^{-2}$ |
| $\varepsilon_{11}$ | $151 \times 10^{-10}$ C (V·m)$^{-1}$ |
| $\varepsilon_{33}$ | $130 \times 10^{-10}$ C (V·m)$^{-1}$ |

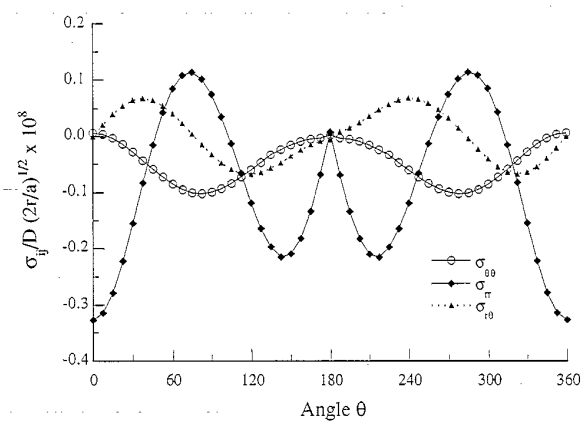


Fig. 3. Angular variations of the stresses $\sigma_{\theta\theta}$, $\sigma_{rr}$ and $\sigma_{r\theta}$ at the crack tip for the applied positive electric field under plane strain condition and for the mechanical boundary conditions at the crack surfaces as defined by 1; $r$, $a$ and angle $\theta$ are defined in Fig. 1. The stresses were normalized by the equivalent electrical displacement $D$ ($= \varepsilon_{33} \times E$) corresponding to the applied electric field $E$. The direction of the applied electric field $E$ was parallel to the direction of poling. The plotted stresses are similar to those calculated theoretically by Sosa [6] (Fig. 4) and Pak [7] (Fig. 7(b)) except a normalization factor due to the finite size of the specimen.

### 4.1. Positive electric field

In order to study the stress distributions under positive electric load, an electric potential of $-100$ V was applied on the face AB and the lower face CD was grounded (Fig. 1). Fig. 3 shows the angular distributions of the radial and tangential stresses $\sigma_{\theta\theta}$, $\sigma_{rr}$ and $\sigma_{r\theta}$ under plane strain conditions for the mechanical boundary condition at the crack surface defined by Eq. (1). These stresses are normalized by the factor $1/D\sqrt{2r/a} \times 10^8$, where $D$ is the equivalent electrical displacement corresponding to the applied electric field $E$, i.e., $D = \varepsilon_{33} \times E$. These stress distributions are similar to those calculated theoretically by Sosa for PZT-4 (Fig. 4 in Ref. [6]) and Pak for PZT-5H (Fig. 7(b) in Ref. [7]) except a normalization factor due to the finite size of the DEN specimen. Sosa's and Pak's calculations are valid for a finite size crack in an infinite piezoelectric medium. For a positive applied electric field, the hoop stresses developed are compressive for all values of $\theta$. The maximum value of the negative hoop stress occurs at an angle $\theta \approx 82°$. Fig. 4 shows the deformed mesh of the DEN model for the negative applied electric field. The displacements shown in figures are scaled to produce the deformed shape. The scale factor is one-tenth of the maximum model dimension [20]. For comparison, the difference between the

$y$-displacement of the node at the right-hand side of the crack surface and the $y$-displacement of the node at the right-hand side of the lower crack surface, $d$, is shown in Fig. 4. The crack opening $d$ is $6.612 \times 10^{-9}$ whereas the width of the specimen is 1.0.

Due to the piezoelectric effect, a positive applied electric field causes an increase in the length along the applied electric field direction. Only the upper half of the model on the right hand side, i.e., region I (Fig. 1), is under a positive electric field in the $y$-direction, whereas the total length of the model ($=2b$) on the left hand side (i.e., regions II and III) is under the same magnitude of the applied positive electric field in the $y$-direction, and most of the lower-half region on the right hand side (i.e., region IV) experiences comparatively small electric field. This causes an expansion in the $y$-direction of the regions II and III which is about twice that of the region I and there is a negligible expansion of region IV. The greater expansion in the $y$-direction of regions II and III causes a pulling of the crack tip towards the left hand due to the Poisson effect. Hence, the crack tip moves up, i.e., the $y$-displacement of the crack tip is positive, and it is also pulled slightly towards the left hand side, i.e., $x$-displacement of the crack tip is negative. As the expansion in the $y$-direction of regions II and III is large as compared with that of region IV, there is a crack opening. As shown in Fig. 3, the crack opening stress, i.e., $\sigma_{\theta\theta}$, is zero for $\theta = 0$; hence, the crack does not grow along $\theta = 0$, and this causes a compressive stress in the upper and lower halves near the crack tip due to the compressive effects of the crack opening in the right half, i.e., both upper and lower crack surfaces compress the material in their respective halves.

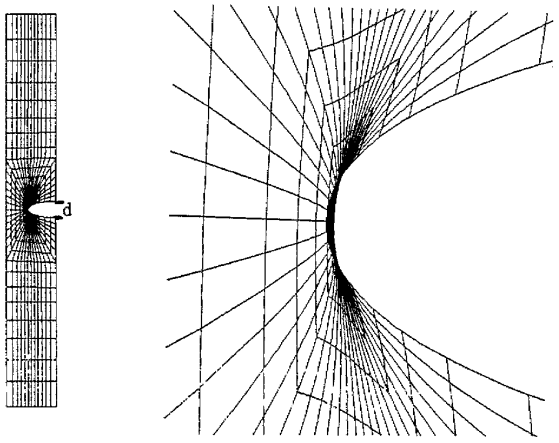


Fig. 4. The deformed mesh of the DEN model for applied positive electric field under the mechanical boundary conditions at the crack surfaces as defined by Eq. (1). The right-hand-side figure is the enlarged view of the deformed mesh near the crack tip. The direction of positive applied field was perpendicular to the crack surface and was the same as the direction of poling. See text for the magnification factor of the displacement shown. The relative displacement $d$ shown in the figure is equal to $6.612 \times 10^{-9}$ whereas the width of the specimen is 1.0.

### 4.2. Negative electric field

An electric potential of $+100$ V was applied on the face AB and the lower face CD was grounded in order to study the stress distributions under negative electric load (Fig. 1). Fig. 5 shows the angular distributions of the radial and tangential stresses $\sigma_{\theta\theta}$, $\sigma_{rr}$ and $\sigma_{r\theta}$ under plane strain condition for the mechanical boundary condition at the crack surface defined by Eq. (1). These stresses are the negative of the stresses developed for positive applied electric field (Fig. 3). For a negative applied electric field, the hoop stresses developed are tensile for all $\theta$. The maximum value of the tensile hoop stress occurs at an angle $\theta \approx 82°$. Hence, this will cause the crack to propagate in an oblique direction.

Fig. 6 shows the deformed mesh of the DEN model for the negative applied electric field. As the effect of a negative applied electric field on the model would be the opposite of that of a positive applied electric field, the crack closure under a negative applied field can be explained along the same lines as the crack opening under a positive applied electric field described in Section 4.1. Due to the piezoelectric effect, there would be a decrease in the length of the model in the $y$-direction under a negative applied electric field. As the total length ($=2b$) of the model in regions II and III is under the negative applied electric field, and the upper half (region I) and lower half (region IV) on the right hand side are under the same negative applied eletric field and a very small electric field, respectively, there is a decrease of the length in the $y$-direction of regions II and III, and this decrease is about twice of the decrease in length in the $y$-direction of region I. In the lower half, in the right hand side (region IV), there is a very small decrease in the length along the $y$-direction. This causes a positive $x$-displacement and a negative $y$-displacement of the crack tip, i.e., the crack tip moves to the right and dips in the $y$-direction. Also, the $y$-displacements of the nodes at the upper and lower crack surfaces are negative. However, the magnitude of the negative $y$-displacement of a node at the upper crack surface is more than that of the corresponding node (i.e., having the same $x$ and $y$ coordinates in the undeformed mesh) at the lower crack surface, and this causes the upper crack surface to go under the lower crack surface. As shown in Fig. 5, the crack opening stress, i.e., $\sigma_{\theta\theta}$, is zero for $\theta = 0$; hence, the crack does not grow along $\theta = 0$ and this causes a tensile stresses in the upper and lower halves near the crack tip due to the tensile effects of the crack closure in the right half, i.e., both upper and lower crack surfaces tries to elongate the material in their respective halves. This also

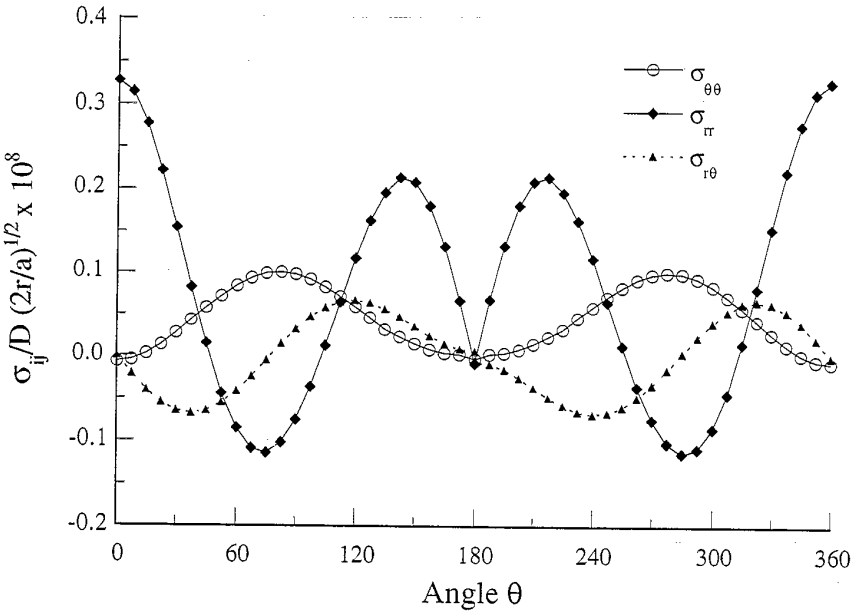


Fig. 5. Angular variations of the stresses $\sigma_{\theta\theta}$, $\sigma_{rr}$ and $\sigma_{r\theta}$ at the crack tip for applied negative electric field under plane strain conditions and for the mechanical boundary conditions at the crack surfaces as defined by Eq. (1); $r$, $a$ and angle $\theta$ are defined in Fig. 1. The stresses were normalized by the equivalent electrical displacement $D$ ($= \varepsilon_{33} \times E$) corresponding to the applied electric field $E$. The direction of the applied electric field $E$ was opposite to the direction of poling.

causes the hoop stress to be maximum at an oblique angle, $\theta$. Hence, the assumption of crack surfaces to be free of surface traction as the mechanical boundary condition is not valid for the negative applied electric field.

### 4.3. Physical interpretation

The deformation of the DEN specimen near the crack tip under positive and negative electric field can be explained with the help of Fig. 7(a) and (b). Due to the increase in the electric field in the uncracked region in the neighborhood of the crack tip, the uncracked region has a tendency to elongate more in the $y$-direction relative to the cracked region (where the electric field is almost zero) for a positive applied electric field.

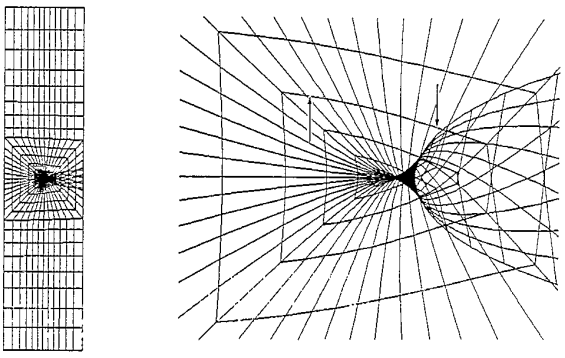

Fig. 6. The deformed mesh of the DEN model for applied negative electric field under the mechanical boundary conditions at the crack surfaces as defined by Fig. 1. The right-hand-side figure is the enlarged view of the deformed mesh near the crack tip. The direction of negative applied field was perpendicular to the crack surface and was opposite to the direction of poling. See text for the magnification factor of the displacement shown.

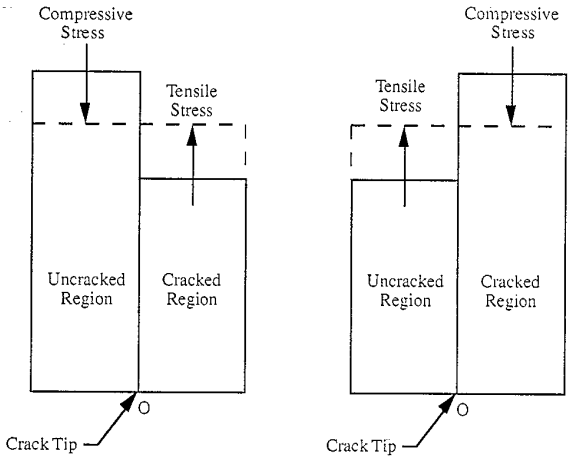


Fig. 7. Physical interpretation of the deformation of the DEN specimen under applied electric field. Stresses near the crack tip (a) for a positive applied electric field and (b) for a negative applied electric field. Solid and dashed horizontal lines denote the free and constrained elongations, respectively, in the $y$-direction.

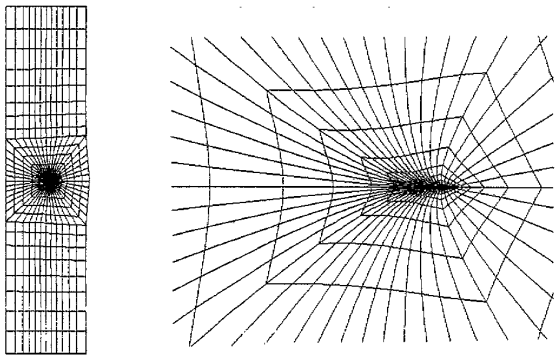

Fig. 8. The deformed mesh of the DEN model for applied negative electric field under the mechanical boundary conditions at the crack surfaces as defined by Eqs. (18) and (19). The right-hand-side figure is the enlarged view of the deformed mesh near the crack tip. The direction of negative applied field was perpendicular to the crack surface and was opposite to the direction of poling. See text for the magnification factor of the displacement shown.

This results in compressive stress in the uncracked region and tensile stress in the cracked region for the positive applied electric field. The reverse stresses will develop under a negative electric field. The right-hand side figure in Fig. 6 clearly shows the effects of the tensile and compressive stress fields in the uncracked and cracked regions, respectively. The deformed line, marked by two arrows, was parallel to the crack in the undeformed mesh.

### *4.4. Mechanical boundary condition at the crack surface*

As we have seen in the last section, the surface traction free mechanical boundary condition defined by Eq. (1) for the crack surfaces is not valid for the negative applied electric field. In this case, electric field causes the crack surfaces to close. Hence, we modified the mechanical boundary condition for the crack surfaces for the negative applied electric field and used the following equation for the displacement field at the crack surfaces (Fig. 1),

$$u_y(x, b^-) = u_y(x, b^+), \quad x > (c - a) \tag{18}$$

where, $b^-$ and $b^+$ denote the lower and upper crack surfaces, respectively, and $u_y(x, y)$ is the $y$-displacement at $(x, y)$. Apart from Eq. (18), we assumed that the shear stress along the crack surfaces is zero, i.e.,

$$\sigma_{r\theta} = 0 \tag{19}$$

Fig. 8 shows the deformed mesh for the negative applied electric field under the new mechanical boundary conditions at the crack surfaces. Fig. 9 shows the angular distributions of the radial and tangential stresses $\sigma_{\theta\theta}$, $\sigma_{rr}$ and $\sigma_{r\theta}$ at the crack tip for the negative applied electric field. As shown in Fig. 9, the hoop stress $\sigma_{\theta\theta}$ is tensile in nature for the negative applied electric field. The hoop stress is maximum at $\theta = 0°$ (as compared with at $\theta \neq 0°$ in Fig. 6 for the mechanical boundary condition defined by Eq. (1)). This will predict the propagation of the crack in a straight line (rather than at an oblique direction, for the mechanical boundary condition of Eq. (1)). Also, under this new mechanical boundary condition at the crack surfaces, the magnitude of the maximum hoop stress is much higher than those under mechanical boundary condition of Eq. (1); hence, the crack will propagate more rapidly. The right-hand side figure in Fig. 8 clearly shows the effect of the highly tensile stress region near the crack tip. Under these new mechanical boundary conditions too, the hoop stress, $\sigma_{\theta\theta}$, at the crack surfaces are zero although we restricted only the $y$-displacements of the two crack surfaces to be the same.

## 5. Conclusions

The two-dimensional finite element technique was used to study the angular distributions of the radial and tangential stresses $\sigma_{\theta\theta}$, $\sigma_{rr}$ and $\sigma_{r\theta}$ at the crack tip under the applied electrical loads on a double edge-notched specimen. The crack surface was assumed to be perpendicular to the poling direction. Electric fields were applied along the poling direction. The calculated stress distributions were in conformity with those predicted by the theoretical analyses of Sosa [6] and Pak [7]. For the negative applied electric field, the analysis of the deformed mesh showed that the mechanical boundary

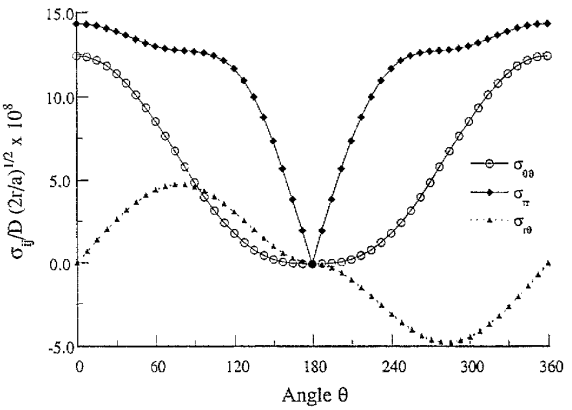


Fig. 9. Angular variations of the stresses $\sigma_{\theta\theta}$, $\sigma_{rr}$ and $\sigma_{r\theta}$ at the crack tip for applied negative electric field under plane strain conditions and for the mechanical boundary conditions at the crack surfaces as defined by Eqs. (18) and (19); $r$, $a$ and angle $\theta$ are defined in Fig. 1. The stresses were normalized by the equivalent electrical displacement $D$ ($= \varepsilon_{33} \times E$) corresponding to the applied electric field $E$. The direction of the applied electric field $E$ was opposite to the direction of poling.

condition at the crack surfaces defined by Eq. (1) (i.e., crack surfaces to be free of surface traction) only was not valid. For a negative applied electric field, the crack tended to propagate in a straight line under the mechanical boundary condition at the crack surface defined by Eqs. (18) and (19) (i.e., for a closed crack), rather than at an oblique angle predicted under the mechanical boundary condition of Eq. (1) only.

## Acknowledgements

Computational assistance on the Cray Y-MP8/864 computer at the Ohio Supercomputer Center, Columbus, Ohio, is gratefully acknowledged. We would like to thank the reviewer for helpful suggestions. This project was supported by the National Science Foundation through a grant No. DMR-9522504.

## References

[1] W.F. Deeg, The analysis of dislocation, crack and inclusion problems in piezoelectric solids, Ph.D. Thesis, Stanford University, CA, 1980.
[2] S. Li, W. Cao, L.E. Cross, Stress and electric displacement distribution near Griffith's type III crack tips in piezoceramics, Materials Letters 10 (1990) 219.
[3] Y.E. Pak, Crack extension force in a piezoelectric material, Journal of Applied Mechanics 57 (1990) 647.
[4] H.A. Sosa, Y.E. Pak, Three-dimensional eigenfunction analysis of a crack in a piezoelectric material, International Journal of Solids and Structures 26 (1990) 1.
[5] H. Sosa, Plane problems in piezoelectric media with defects, International Journal of Solids and Structures 28 (1991) 491.
[6] H. Sosa, On the fracture mechanics of piezoelectric solids, International Journal of Solids and Structures 29 (1992) 2613.
[7] Y.E. Pak, Linear electroelastic fracture mechanics of piezoelectric materials, International Journal of Fracture 54 (1992) 79.
[8] B. Wang, Three-dimensional analysis of a flat elliptical crack in a piezoelectric material, International Journal of Engineering Science 6 (1992) 781.
[9] V.Z. Parton, Fracture mechanics of piezoelectric materials, Acta Astronautica. 3 (1976) 671.
[10] T.Y. Zhang, J.E. Hack, Mode-III cracks in piezoelectric materials, Journal of Applied Physics 71 (1992) 5865.
[11] T.H. Hao, Z.Y. Shen, A new electric boundary condition of electric fracture mechanics and its applications, Engineering Fracture Mechanics 47 (1994) 793.
[12] M.L. Dunn, The effects of crack face boundary conditions on the fracture mechanics of piezoelectric solids, Engineering Fracture Mechanics 48 (1994) 25.
[13] S. Kumar, R.N. Singh, Crack propagation in piezoelectric materials under combined mechanical and electrical loadings, Acta Metallurgica et Materialia 44 (1996) 173.
[14] S. Kumar, R.N. Singh, Energy release rate and crack propagation in piezoelectric materials. Part I—Mechanical/electrical load, Acta Materialia 45 (1997) 849.
[15] S. Kumar, R.N. Singh, Energy release rate and crack propagation in piezoelectric materials. Part II—Combined mechanical and electrical loads, Acta Materialia 45 (1997) 859.
[16] H. Wang, R.N. Singh, Piezoelectric ceramics and ceramic composites for intelligent mechanical behaviors, Ceramic Transactions 43 (1994) 277.
[17] H. Wang, R.N. Singh, Crack propagation in piezoelectric ceramics: II, Effects of applied electric fields, Journal of Applied Physics (1997) in press.
[18] T.L. Anderson, *Fracture Mechanics: Fundamentals and Applications*, CRC Press, Boston, 1991.
[19] ABAQUS Version 5.4, Hibbitt, Karlsson and Sorensen Inc., Pawtucket, RI, 1995.
[20] ABAQUS/Post Manual Version 5.3, Hibbitt, Karlsson and Sorensen Inc., Pawtucket, RI, 1993.